Cell Reports
Physical Science

CellPress
OPEN ACCESS

Article

High-strength, lightweight nano-architected silica

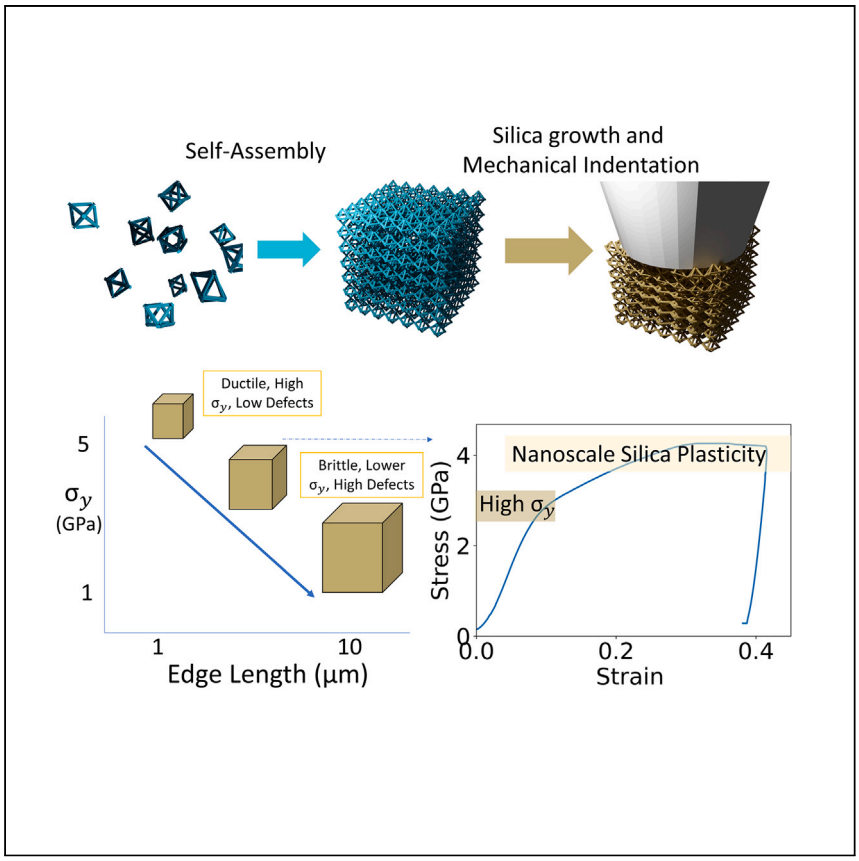

Michelson et al. demonstrate the fabrication of 3D silica nanostructures via DNA assembly and templating, where nanostructures show a nearly theoretical compressive strength of 5 GPa. DNA nanotechnology opens the opportunity to engineer 3D materials for exploring and exploiting nanoscale mechanical effects.

Aaron Michelson, Tyler J. Flanagan, Seok-Woo Lee, Oleg Gang

seok-woo.lee@uconn.edu (S.-W.L.)
og2226@columbia.edu (O.G.)

Highlights

Fabrication of 3D silica nanostructures via DNA assembly and templating

In situ micro-compression testing to examine the mechanical properties

Nanostructures show a nearly theoretical compressive strength of 5 GPa

Michelson et al., Cell Reports Physical Science 4, 101475
July 19, 2023
https://doi.org/10.1016/j.xcrp.2023.101475

Cell Reports
Physical Science

CellPress
OPEN ACCESS

Article

High-strength, lightweight nano-architected silica

Aaron Michelson,[1,2,3] Tyler J. Flanagan,[4] Seok-Woo Lee,[4,*] and Oleg Gang[1,2,3,5,*]

SUMMARY

Continuous nanolattices are an emerging class of mechanical metamaterials that are highly attractive due to their superior strength-to-weight ratios, which originate from their spatial architectures and nanoscale-sized elements possessing near-theoretical strength. Rational design of frameworks remains challenging below 50 nm because of limited methods to arrange small elements into complex architectures. Here, we fabricate silica frameworks with ~4- to 20-nm-thick elements using self-assembly and silica templating of DNA origami nanolattices and perform *in situ* micro-compression testing to examine the mechanical properties. We observe strong effects of lattice dimensions on yield strength (σ_y) and failure mode. Silica nanolattices are found to exhibit yield strengths higher than those of any known engineering materials with similar mass density. The robust coordination of the nanothin and strong silica elements leads to the combination of lightweight and high-strength framework materials offering an effective strategy for the fabrication of nanoarchitected materials with superior mechanical properties.

INTRODUCTION

One of the longest-held pursuits of materials science and engineering has been the production of lightweight, mechanically robust materials. In recent years, the advancements in top-down and bottom-up fabrications have allowed for the construction of 3D meso- and nanoscale periodic architected structures, which are often referred to as meso-nano-lattices.[1–6] Because a lattice consists of repeating motifs of individual unit cells, the strength of these materials is determined by a complex combination of the structure's constituent materials, the unit cell structure, and the length and width of the individual elements, or struts, of the lattice.[3,7–10] In addition to lattice effects, nanoscale lattices typically possess high strength-to-weight ratios because their nanosized elements exhibit ultrahigh strength due to the mechanical size effect, or so-called "smaller is stronger" behavior.[11–18] Sometimes, it is even possible to obtain a yield strength higher than their corresponding fully dense bulk solids when the size effect is stronger than the density effect.[19]

Due to the superior strength-to-weight ratio, nanolattices can provide a mechanically robust open framework for several potential applications. Self-assembled nanolattices as a sputtering template have allowed for the creation of a 3D superconducting architected structure as well as nanoengineered oxide structures for battery materials.[20,21] Moreover, incorporation of functional nanoparticles into a lattice enables nanostructured catalysis platforms.[22] Self-assembly of nanoparticles using such platforms has yielded applications toward broadband absorption surfaces,[23] memory devices,[24] and sensors.[25] The possibility to generate nanostructures for creating robust materials, as inspired by biomineralization, allows for extending applications as a biomaterial for bone or scaffolded tissue growth.[26,27]

[1]Department of Chemical Engineering, Columbia University, 817 SW Mudd, New York, NY 10027, USA

[2]Department of Applied Physics and Applied Mathematics, Columbia University, New York, NY 10027, USA

[3]Center for Functional Nanomaterials, Brookhaven National Laboratory, Upton, NY 11973, USA

[4]Department of Materials Science and Engineering & Institute of Materials Science, University of Connecticut, 97 North Eagleville Road, Unit 3136, Storrs, CT 06269-3136, USA

[5]Lead contact

*Correspondence: seok-woo.lee@uconn.edu (S.-W.L.), og2226@columbia.edu (O.G.)

https://doi.org/10.1016/j.xcrp.2023.101475

All these applications certainly require the structural stability of nanolattices. Therefore, there is a significant need to develop effective methods that enable rational design and fabrication of nanolattices with excellent mechanical properties that eventually guarantee reliable performance for engineering devices. Moreover, for a responsive nature of lattice elements, the prospect exists for establishing material with dynamic and switchable mechanical behavior.[28,29]

The strength-to-weight ratio of nanolattices is strongly related to the dimensions of the element sizes. At the nanoscale, a material often exhibits a significant fraction of theoretical strength due to the absence of defects, such as dislocations or cracks. This is the reason why a nanowire or nanoparticle exhibits extremely high strengths. For a given relative density and structural form of nanolattices, therefore, it is desirable to have a thinner element that could possess higher strength according to the size effect. To obtain this benefit, 3D photolithography has been extensively used with a multitude of techniques, such as pyrolysis, atomic layer deposition, and electroplating.[18,20] While photolithography methods are effective in the production of planar structures, they are quite time consuming and are limited in their ability to produce architected 3D organization. In addition, producing nanoscale features below 50 nm is challenging, which limits the benefits of the size effect. Therefore, novel fabrication strategies are required for generating designed 3D nanostructured materials via bottom-up fabrication. Such materials should consist of extremely thin elements and would allow for creating continuous nanolattices (frameworks) with a significantly enhanced strength-to-weight ratio.

In recent years, DNA frames have been demonstrated as essential nanoscale blocks to form a wide variety of nanoarchitectures starting from individual polyhedral frames.[30] The frames are a DNA molecule formed by folding a long single strand of DNA with many small "staple" strands, which twist and shape the long sequence into a pre-defined shape. This so-called DNA origami approach[31] allows us to form engineered 3D shapes.[32] The frame shape is encoded further with sequences at vertices that pair with a neighboring frame to form extended nanolattices.[33] Internal staple strands not involved in the macroscopic assembly can be switched out to allow for addressing individual frames for further pairing with DNA-functionalized nanoparticles or other tags. The connectivity of these structures depends on the design of frames and their connectivity, which makes a variety of lattice types possible for assembly and exploration. These ordered DNA frameworks can furthermore be transitioned to the solid state via sol-gel synthesis of silica and more complex material compositions,[6,34–36] which produces the elements with 10–20 nm in thickness, below the limit of photolithography-generated nanolattices.[1] The DNA-programmable assembly offers a high-throughput technique that can be potentially scaled up with the falling cost of DNA oligonucleotides.[37] The time to produce a large number of high-quality origami and subsequent lattices ranges from hours[38] to days[39] and can be reduced through optimizing kinetic effects, and the structure can be engineered with high uniformity.[40] The structural similarity of the DNA-based framework nanolattice to those proposed by these models positions it uniquely to potentially achieve lightweight and high-strength materials.

In this study, we investigated self-assembled cuboid DNA silica frameworks with the octahedron coordination of 4- to 20-nm-thick elements, and their mechanical properties were investigated using *in situ* micro-compression in a scanning electron microscope (SEM). This lattice has an average coordination of struts of 8, which is above that required for rigidity of Maxwell lattices, which typically have coordination z, twice the dimensionality of the strut design.[41] We found a strong effect of lattice

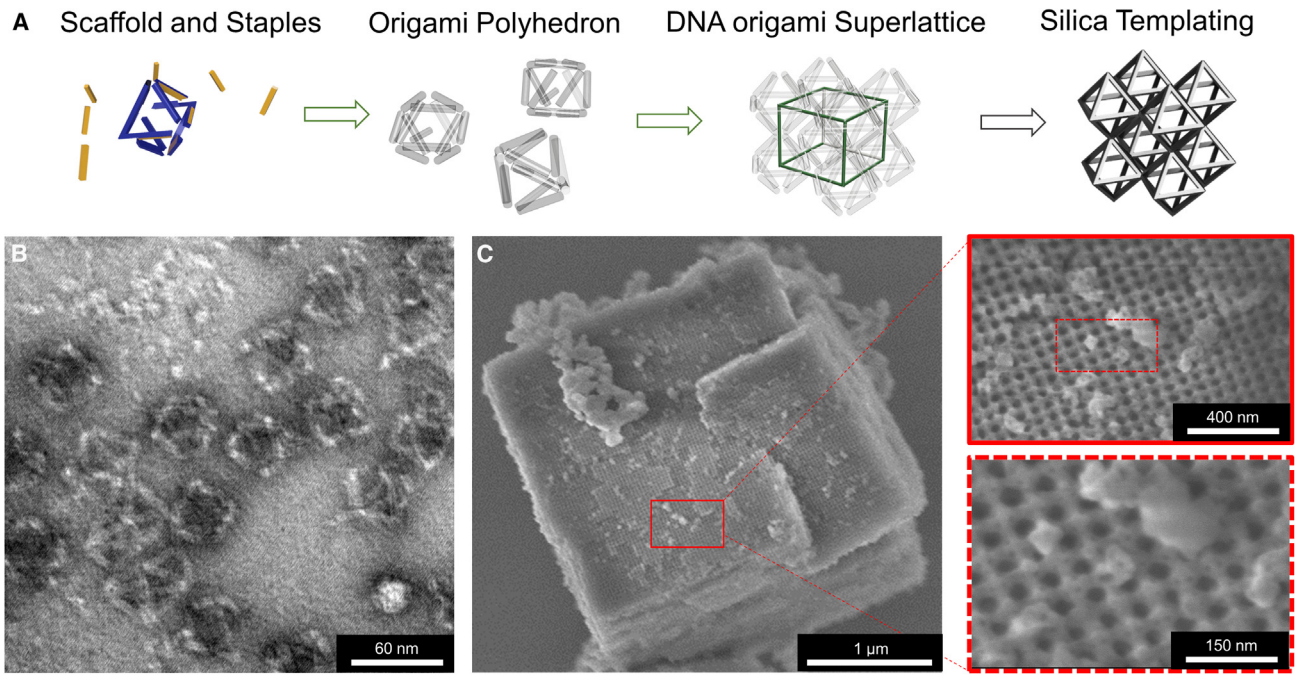

Figure 1. Silica framework synthesis

(A) DNA origami to silica ordered framework synthesis schematic.

(B) TEM micrograph of DNA origami frame prior to nanolattice assembly.

(C) SEM micrograph of a framework sample at higher magnification and at low magnification wherein multiple octahedral frames can be visualized.

dimension on yield strength and failure mode. Advanced electron microscopy revealed that the effect of lattice dimension is strongly related to the presence of lattice defects. Surprisingly, all silica nanolattices in this study exhibit yield strength much higher than any other engineering materials with a similar mass density, with the best performance close to the theoretical maximum. These results imply that DNA self-assembly technique offers a flexible pathway to fabricate mechanically robust materials through engineering nanoscale architecture and composition.

RESULTS AND DISCUSSION

Fabrication of silica nanolattices

Fabrication of DNA-based cuboid silica nanolattices starts with a single DNA octahedron, which has an edge length of approximately ~29 nm (Figures 1A and 1B). The octahedron frames form nanolattice structures by the vertex-to-vertex connections between the frames. Each octahedron is coordinated with 6 neighboring octahedrons with complementary DNA at the vertices. The DNA octahedron unit structure repeats in space to yield a cubic nanolattice with an edge length varying between 1 and 10 μm (Figure 1C). Nanolattices are then coated with silica using a sol-gel process using (3-aminopropyl) triethoxysilane (APTES) and tetraethyl orthosilicate (TEOS).[34,36] The thickness of the silica coating is on the order of 2–10 nm radially around the DNA strut, yielding 4- to 20-nm-thick struts in diameter. The details of nanolattice fabrication are available in the experimental procedures. Note that we intentionally chose the octahedron-structured nanolattice because its stretching-dominant deformation behavior guarantees superior yield strength[8,15,42]; however, we note that the achieved density of the samples likely means that there are shared contributions of stretching and bending deformation in the samples.

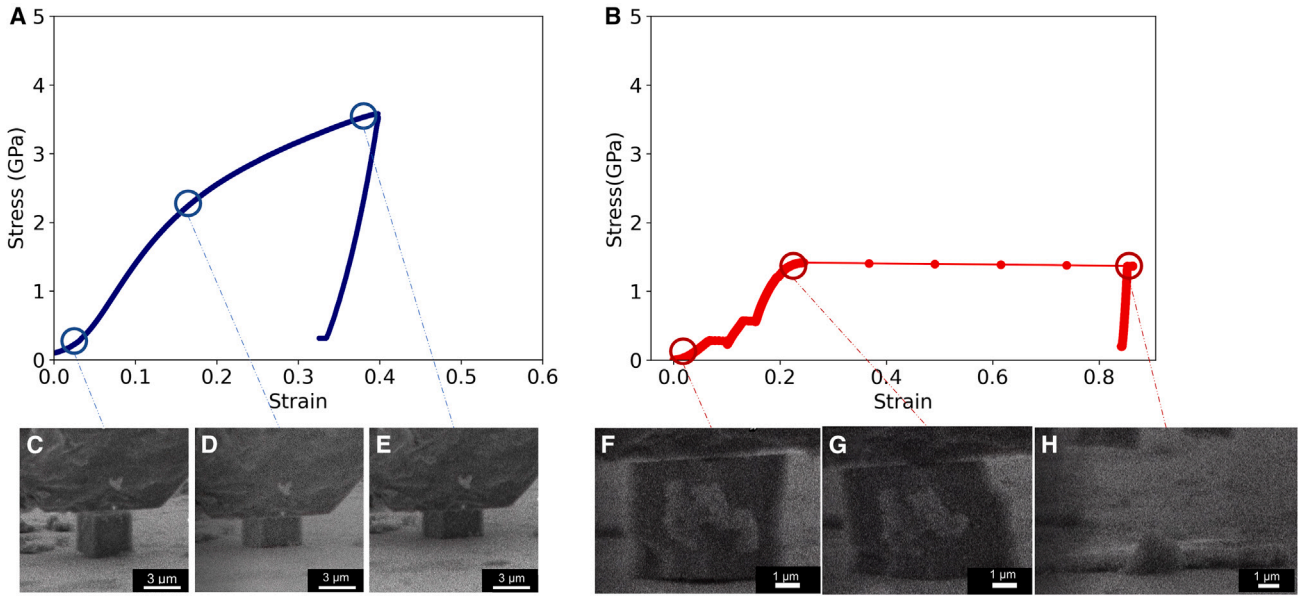

Figure 2. Ductile and brittle deformation

(A) Representative compressive stress-strain curve for a framework nanolattice with an edge length of 3 μm.

(B) Compressive stress-strain curve for a large nanolattice with a 6-μm edge length.

(C–E) Correlative SEM images from *in situ* mechanical compression of the nanolattice showing initial, yield point, and final compressed state.

(F–H) Correlative SEM images from the initial state, yield point, and final nanolattice state wherein a brittle bursting deformation process took place.

Ductile and brittle deformation

The synthesis yield of a single batch of nanolattices is quite high, providing a large number of lattices of varying sizes. The lattices tend to cluster in large mounds (10–100) with a few isolated lattices located in between. Of these isolated particles, only those of a cuboid geometry were selected for micro-compression testing. To this end, samples within a size range of 1.2–8 μm were compressed, with the majority of lattices tested clustering around 3 μm. The cubic geometry of the nanolattice allowed for the direct uniaxial compression of nanolattices sitting upright on a silicon substrate. Small nanolattices (edge length < 3 μm) with a high yield strength of above 2 GPa typically yielded a significant plastic deformation (Figures 2A, 2B, and S8; Videos S1 and S2). Large nanolattices (edge length > 3 μm) tended to fail with one or two sudden bursts (Figures 2C and 2D) wherein little to no plastic deformation occurred in the sample prior to fracture. About 54% of large nanolattices exhibited complete brittle fracture. It is interesting that small nanolattices exhibit ductile deformation since, traditionally, silica is known as a very brittle material. We believe that this ductile deformation originates from the nanoscale size effect of the silica coating the structure. It has been reported that silica nanofibers undergo a size-dependent brittle-to-ductile transition at diameters below 18 nm.[43] The study postulated that the increase in relative surface area due to the extremely small diameter of the fibers allows for dangling oxygen bonds to quickly move to uncoordinated Si atoms, forming new Si–O bonds as the sample undergoes tension and the original bonds are broken. If the rate of this bond-switching process exceeds irreversible bond loss, flaws can be blunted, and the entire sample can be deformed via shear banding instead of crack propagation. It was also noted that at ~5-nm diameter, the fibers were capable of 18% elongation before failure, a similar diameter to that of the octahedral struts in this study.

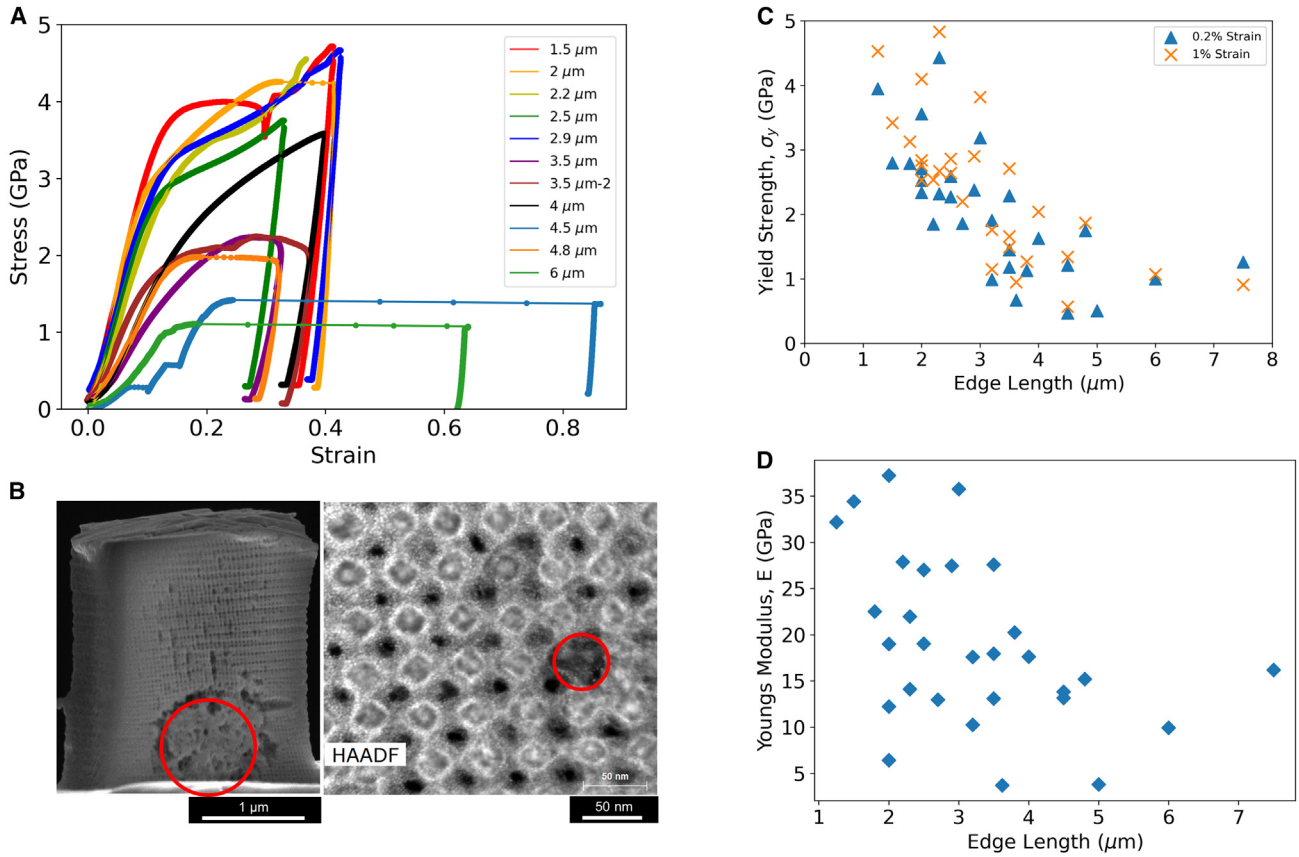

Figure 3. Size effect and nanoscale defects

(A) Stress-strain curve of lattice ranging in size from 1.5 to 6 μm in edge length, with larger lattices tending toward yielding at lower strength.

(B) A cross-section image of a nanolattice reveals voids and disordered regions (left) and nanovacancies (right).

(C) A plot of compressive yield strength vs. size of the lattice displaying a tendency for smaller lattices to have higher yield strength reaching above 3 GPa. Yield strength for both a 0.2% and 1% strain offsets are shown.

(D) Young's modulus vs. size showing a range from 37 down to <5 GPa as calculated from a fit of the stress-strain curve.

The diameters of our strut members range between 4 and 20 nm, as estimated from direct cross-section measurement (Figures S3–S6), and the ductility seen under compression thus suggests that the silica in our smaller samples undergo shear deformation. However, the large nanolattices exhibit brittle fracture even though the structure and dimensions of the octahedron unit cell do not change. This result implies the presence of other factors such as lattice defects, which could induce crack initiation and propagation at lower stress levels. An early consideration is that surfaces of nanolattices that do not present an atomically flat surface for contact with the indenter act as stress concentration points. The irregularity of the surface or direct misalignment from perfectly flat to the indenter are corrected after initial contact with the indenter, which is present in the data as a low slope at the very beginning of the stress-strain data (see Figures S7 and S8). Both Young's modulus and yield strength were obtained from the stress-strain data measured after full contact.

Size-dependent strength of nanolattices

The presence of defects is indirectly observed in size-dependent yield strength and Young's modulus. Nanolattices show high yield strength using a 1% strain offset[15,44] ranging from 0.5 to 4.8 GPa (Figure 3A, Table S1), and as the edge length of the nanolattice increased, the yield strength decreases (Figure 3B). A similar trend

regarding the Young's modulus is also shown with modulus varying from 30 down to <5 GPa (Figure 3C). The Young's modulus of bulk fused silica has been measured to be ~72 GPa, and it has been observed that the Young's modulus for silica is relatively unaffected by size.[45] One inference that might be made from the apparent decrease in the yield strength is the potential variability of the nanolattice silica coating. However, when examining lattices by focused ion beam (FIB)/SEM cross-section, we could see no large variation in the thickness of the silica growth, which was consistently between 4 and 10 nm. Representative regions can be seen in Figure 3B. Pore size ranging from 15 to 20 nm remained consistent across sample sizes (see Figure S3).

Having interrogated the structure for variations in the thickness and continuity of the silica coating, cross-sectional analysis yielded a direct view of defects within the nanolattices (Figure S6; Table S2), where the most common defects seen were vacancies and voids. This observation suggested that the decreasing yield strength with increasing nanolattice sample size is related to the larger number of defects. Octahedral vacancy occurrences range between 0.07% and 0.8% or 1:125 or 1:1,100 for the lowest defect occurrence. Each octahedral vacancy represents approximately a 0.1% increase in void space. The total defect porosity from large voids and defective regions within the crystal represents between 0.5% and 11% void space. The low Young's modulus for larger nanolattices that exhibited brittle failure can be explained by the presence of these large voids, which most likely contribute to catastrophic failure of the nanolattice. Under compression, friction stresses typically induce barreling around the pore, which introduces lateral tensile stresses that initiate a crack from the pore, thus leading to catastrophic failure under lower stresses (shown in Figure S7 and Video S3).

In light of the flaw-driven process described, we can estimate the critical length scale for fracture in the silica nanolattice compared with the defect-free lattice following Griffiths criterion and the surface energy of fused silica, 3.5–5 J/m^2.[46,47] The estimated critical length scale for silica is 15–22 nm for a theoretical strength of E/10 and 139–200 nm for E/30, respectively. In our case, since the silica thickness is in the range of 4–10 nm, we can assume that the silica struts are flaw insensitive and thus able to reach theoretical strength. This explains the observed high strength of nanolattices with small domain sizes. Both the flaw insensitivity and the enhanced Si–O bond switching at the nanoscale promote high strength and ductility of the relatively homogenous domains.

The visualization of the large disordered region in Figure 3B corresponds to the correlation length of nanolattices obtained from small-angle X-ray scattering (SAXS), which is on the order of 0.5–1 μm (Figure S1). Beyond the correlation length, we would expect that voids and disordered regions like the one visualized are more likely to develop. Octahedron vacancies are easily accommodated in the nanolattice; a missing octahedron in the structure can be circumvented as the nanolattice grows in parallel directions (Figure 3B). This means that the quantity of octahedron vacancies increases with the size of the nanolattice sample due to the stochastic nature of defects forming in larger volume. These two phenomena (vacancies and voids) are likely the root cause for the decrease in the strength with increased nanolattice sample size (Figure 3C); thus, the increase in defect volume creates easy directions for crack propagation and deterioration of stability. This effect resembles a behavior of yield strength for atomic crystalline materials, for which an exponential dependence is observed of the form $\sigma = Ad^{-n}$, where d is the pillar diameter.[14] Although the exponent n cannot be accurately assessed in our case due to the

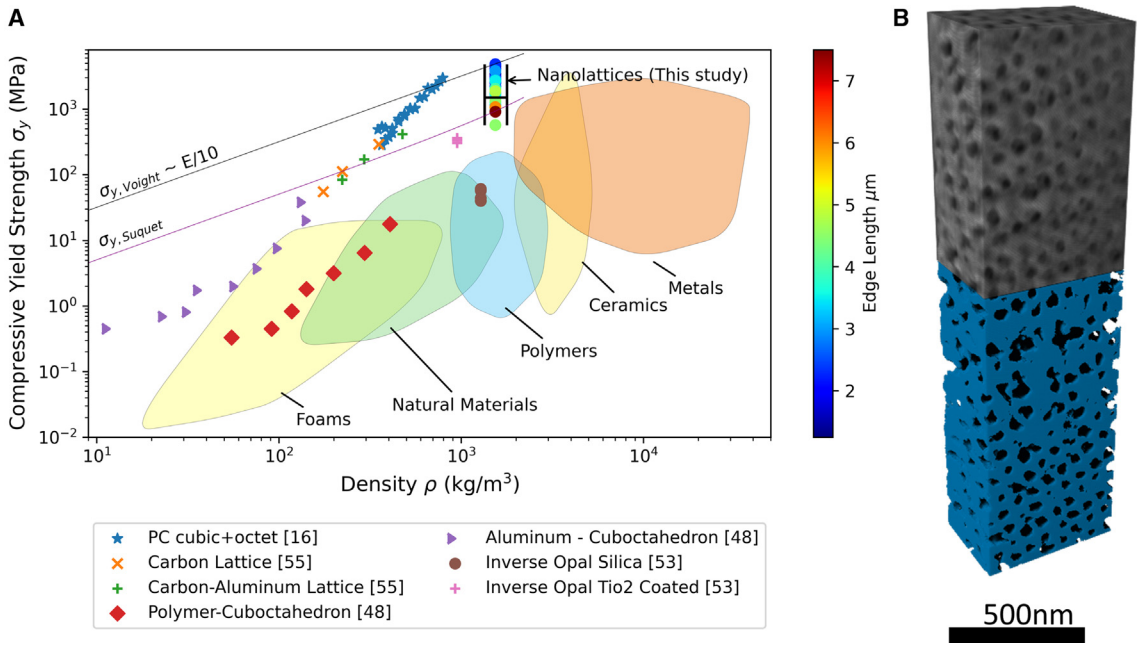

Figure 4. Ashby chart

(A) Compressive strength vs. density plot. Silica framework materials in this study have a density on the order of 2,000 kg/m^3 with yield strength of between 1 and 4.8 GPa, which roughly corresponds with edge length, as shown in Figure 3C. The color coding of framework samples corresponds to their different edge lengths, according to a color bar scale. The findings compare favorably with other nanolattices such as alumina and carbon based, with representative examples shown.

(B) Volumetric density based on serial sectioning of a superlattice using dual-beam FIB. The volume reconstruction of the nanolattice is shown with the top portion of the dataset in grayscale, and the bottom half in blue represents the segmented porous structure based on Otsu thresholding of the intensity.

limited dynamic range of edge length, its estimated value is 0.8–0.9. Additionally, the role of missing beams was studied on nanoscale octet-trusses, where Meza et al. observed an exponential scaling of stiffness, n = 3–3.8, and strength, m = 3.1–4.3, which roughly translates to a factor of 2 decrease in yield strength and stiffness for ~20% missing beams, similar to what is shown in this study.[48] The mechanism described for the weakening of the lattice due to nanovoids and nanopores likely explains the dual modalities of failure noted earlier, with smaller, more defect-free lattices failing with ductile behavior as struts stretch after yielding versus large brittle failure, which exploits weaknesses in the volume of the sample.

Comparison with other types of nanolattices

To compare the compressive strength of the nanolattice against other structures, we assess the density of the obtained lattices, summarized in Figure 4A with an Ashby plot. This was done by extrapolating density directly from volumetric imaging of the structure with electron microscopy and, second, by inspection of the stress-strain curve. From the unit cell, we can approximate a theoretical relative density of an octahedral unit cell geometrically as 12 cylindrical struts in a box, which can be shown for an edge length, l, to be $\rho_{lattice} = \frac{12\pi r^2}{(\sqrt{2}\,l)^2}$. Given an average strut radius, r, of 6–7 nm and an edge length of 29 nm, the total density of a defect-free lattice would be 57%–77% of the bulk material, respectively. This compares well against direct volumetric imaging via serial section reconstruction of a section of nanolattices shown in Figures 4B and S4. The obtained filling fraction value ranges from 66% to 77% depending on the thresholding technique (Otsu thresholding yields 66%). For bulk silica with a density of 2,200 kg/m^3, this would translate to 1,400–1,700 kg/m^3. However, given the

stochastic nature of voids in the assembly process, it is difficult to ascertain the density with a high degree of confidence at the outset.

In a second method, we extrapolated the relative density of each sample by examining $\rho^m \sim E_{lattice}/E_{bulk}$, where m represents the influence of architecture, where stretching-dominant structures are expected to have an $m \sim 1$.[7,18,49,50] The expected scaling for the stiffness of our structure with beam slenderness,[48] $\lambda > 25$, approximately scales with $\rho \propto \left(\frac{r}{l}\right)^2$. Additionally the r/l ratio of ~0.24 suggests that the relative influences of stretching and bending are comparable and that the expected m scaling should be ~2 for the cuboctahedron-type lattice.[48]

In our study, the smallest lattices display Young's moduli approximately 50% that of the bulk (72 GPa), as shown in Figure 3D. Larger nanolattices with higher chances for voids to develop and weaken the structure have correspondingly lower Young's moduli and yield strengths. This effect is reflected in the distribution of measured yield strengths for lattices with different edge lengths (Figure 4A).

Another prominent possibility for the variance in the Young's modulus is that the silica itself formed via sol-gel synthesis. The size effect on silica nanowires is said to rely on a large surface area-to-volume ratio, which leads to elastic stiffening related to surface elasticity, which may depend on the synthesis of the silica itself.[51] The network structure our silica forms is calcined prior to nanoindentation in an attempt to saturate bonds to form SiO_2. However, the decomposition of DNA along with the buffer solutions used to keep DNA stable in solution has a tendency to leave behind various carbon, phosphorous, and nitrogen impurities in the silica network, which likely leaves bonds unsaturated or even creates nanoporosity in the struts of the structure.[35] The effect will be the subject of further examination where varying thicknesses and nanolattice types can better confirm how the architecture affects the scaling of Young's modulus.

When plotting compressive strength vs. density, it becomes clear that the lattices are near the theoretical maximum yield strength, where here we consider the Voigt upper bound ($\sigma_y \sim$ E/10 ~ 7 GPa for silica) and the Suquet upper bound, see Figure S2 for Poisson ratio.[16] For the modulus of bulk fused silica of 72 GPa and 70% filling, the theoretical yield strength can be estimated as 5 GPa.[51,52] Using the direct volumetric calculation for density, the smallest nanolattices displayed σ_y ~4.5 GPa, or 90% theoretical yield strength. Our DNA silica nanolattice is thus competitive in the pantheon of lightweight, high-strength materials, as illustrated in the Ashby plot in Figure 4. Relative to other nanoscale nanolattices[7,16,48,53–55] and meshes, it can be seen that DNA-templated frameworks have a high yield strength nearing the theoretical maximum limit for the given density.

In closing, we have demonstrated that DNA frames assembled in a lattice and templated with silica present a class of engineered mechanical metamaterials with high strength (1–5 GPa) and light weight. Since DNA assembly methods are capable of creating diverse lattice types by modifying a frame geometry and a connectivity of frames, the demonstrated approach opens up a possibility to create materials with different mechanical responses. Moreover, the development of templating methods[6,20,34,35,56] provides a means to exploit different elemental compositions of frameworks. The work will provide a pathway for the creation of mechanically robust nanolattices that can be further coupled with nanoscale functions for future technologies including superconductors, battery cathodes, nanophotonics, and catalysis.

EXPERIMENTAL PROCEDURES

Resource availability

Lead contact

Further Information and requests for resources should be directed to the lead contact, Oleg Gang (og2226@columbia.edu).

Materials availability

Nanolattices generated in this study can be made available on request, but we may require a payment and/or a completed materials transfer agreement if there is potential for commercial application.

Data and code availability

Data can be made available upon reasonable request. Requests should be directed to the lead contact.

Synthesis

DNA origami and AuNP-nanolattice assembly

DNA-origami octahedrons[39] (see Note S1) were formed by mixing M13mp18 DNA scaffold and DNA staple strands with a 1:5 ratio in 1× TAE buffer (40 mM Tris acetate, 1 mM EDTA) with 12.5 mM Mg^{2+} and being slowly annealed from 90°C to room temperature over the course of 20 h for origami formation, overall a −0.2 C/h ramp rate. Nanolattices of DNA origami were formed by mixing two DNA octahedrons with complementary DNA bases at the vertices. The origami was then mixed to form a 20 nM concentration solution at 20–50 μL. The sample was annealed in a PCR over 5 days from 50°C to room temperature (RT) at −0.2°/h.

Silica mineralization

Robust DNA origami nanolattices were made by growing a layer of silica on the DNA bundle. For conversion to inorganic silica, nanolattices were centrifuged, and supernatant was replaced with 0.1× TAE with 10 mM Mg. Separately, silication buffer was prepared by adding 2.5 μL APTES and 10 μL TEOS in 0.1× TAE with 10 mM Mg buffer for a total volume of 500 μL. The solution was vortexed at 700 rpm for 30 min and filtered with a 0.22 μm Millex-GV PVDF filter to remove large particulates, and then 5 μL nanolattice and 10 μL silication buffer were mixed in a tube. The solution was vortexed at 700 rpm for 1–2 h and then centrifuged and buffer exchanged with water. Structural confirmation of the structure using SAXS (see Figure S1) showed the resultant superlattice structure corresponded to a simple cubic structure factor with a lattice parameter of 49 nm. The sample was drop casted onto a silica wafer and then annealed at 500°C to remove DNA and fully convert the lattice to silicon dioxide.

Samples were sectioned to evaluate their porosity using the Helios 650 series FIB/SEM. The images can be seen in Figure S3. The cutting was performed at 30 KeV and 28 pA beam current. Samples were cut to approximately half their volume. Pores were measured manually using ImageJ. Volumetric reconstruction from serial sectioning of nanolattices was performed at CUNY ASRC FIB/SEM and is described in Figure S4.

In situ *compression test*

Compression tests were performed on two *in situ* micro-mechanical testing systems. The first system was a combination of a JEOL 6335F field-emission gun SEM (JEOL, Tokyo, Japan) for imaging and micro-mechanical compression testing performed *in situ* using a NanoFlip system (KLA, Milpitas, CA, USA) outfitted with a 15-μm-diameter diamond flat-punch tip. The second system was an FEI Helios FIB/SEM for

imaging and a micro-mechanical testing device, FT-NMT04 (Femtotools, Buchs, Switzerland), with a 5-μm-diameter diamond flat-punch tip.

Only isolated nanolattices with a cuboid geometry and flat orientation were chosen for compression. The lattices were compressed with a nominal displacement rate of 10 nm/s, which corresponds to an approximate strain rate of $10^{-3}\ s^{-1}$. Samples were loaded until failure in the case of brittle samples and to ~40% plastic strain in the case of ductile deformation. The yield strength was estimated using either a 0.2% or 1% strain offset from the linear portion of the stress-strain curve.

SUPPLEMENTAL INFORMATION

Supplemental information can be found online at https://doi.org/10.1016/j.xcrp.2023.101475.

ACKNOWLEDGMENTS

This research used resources of the Center for Functional Nanomaterials, and small-angle scattering was collected at the Complex Matter Scattering (CMS) at 11-BM of the National Synchrotron Light Source II at Brookhaven National Laboratory, which are of the US DOE Office of Science Facilities, under contract no. DE-SC0012704. The DNA assembly work was supported by the US Department of Energy, Office of Basic Energy Sciences, grant DE-SC0008772. The material fabrication and characterization work was supported by the US Department of Defense, Army Research Office, W911NF-19-1-0395.

AUTHOR CONTRIBUTIONS

O.G., S.-W.L., A.M., and T.J.F. conceived concept. A.M. prepared DNA-based lattices. A.M. and T.J.F. conducted indentation experiments. A.M. and T.J.F. analyzed data. S.-W.L., O.G., A.M., and T.J.F. prepared the manuscript.

DECLARATION OF INTERESTS

The authors declare no competing interests.

Received: January 31, 2023
Revised: May 15, 2023
Accepted: June 6, 2023
Published: June 27, 2023

REFERENCES

1. Lewis, J. (2006). Direct ink writing of 3D functional materials. Adv. Funct. Mater. *16*, 2193–2204. https://doi.org/10.1002/adfm.200600434.

2. Jang, D., Meza, L.R., Greer, F., and Greer, J.R. (2013). Fabrication and deformation of three-dimensional hollow ceramic nanostructures. Nat. Mater. *12*, 893–898. https://doi.org/10.1038/nmat3738.

3. Muth, J.T., Dixon, P.G., Woish, L., Gibson, L.J., and Lewis, J.A. (2017). Architected cellular ceramics with tailored stiffness via direct foam writing. Proc. Natl. Acad. Sci. USA *114*, 1832–1837. https://doi.org/10.1073/pnas.1616769114.

4. Tian, Y., Lhermitte, J.R., Bai, L., Vo, T., Xin, H.L., Li, H., Li, R., Fukuto, M., Yager, K.G., Kahn, J.S., et al. (2020). Ordered three-dimensional nanomaterials using DNA-prescribed and valence-controlled material voxels. Nat. Mater. *19*, 789–796.

5. Ma, N., Minevich, B., Liu, J., Ji, M., Tian, Y., and Gang, O. (2020). Directional assembly of nanoparticles by DNA shapes: towards designed architectures and functionality. Top. Curr. Chem. *378*, 36.

6. Michelson, A., Minevich, B., Emamy, H., Huang, X., Chu, Y.S., Yan, H., and Gang, O. (2022). Three-dimensional visualization of nanoparticle lattices and multimaterial frameworks. Science *376*, 203–207. https://doi.org/10.1126/science.abk0463.

7. Meza, L.R., Das, S., and Greer, J.R. (2014). Strong, lightweight, and recoverable three-dimensional ceramic nanolattices. Science *345*, 1322–1326.

8. Huber, N. (2018). Connections between topology and macroscopic mechanical properties of three-dimensional open-pore materials. Front. Mater. *5*. https://doi.org/10.3389/fmats.2018.00069.

9. Greer, J.R., and Deshpande, V.S. (2019). Three-dimensional architected materials and structures: design, fabrication, and mechanical behavior. MRS Bull. *44*, 750–757. https://doi.org/10.1557/mrs.2019.232.

10. Mueller, J., Raney, J.R., Shea, K., and Lewis, J.A. (2018). Architected lattices with high stiffness and toughness via multicore–shell 3D printing. Adv. Mater. *30*, 1705001. https://doi.org/10.1002/adma.201705001.

11. Zhu, T., and Li, J. (2010). Ultra-strength materials. Prog. Mater. Sci. *55*, 710–757.

12. Uchic, M.D., Shade, P.A., and Dimiduk, D.M. (2009). Plasticity of micrometer-scale single crystals in compression. Annu. Rev. Mater. Res. *39*, 361–386.

13. Kraft, O., Gruber, P.A., Mönig, R., and Weygand, D. (2010). Plasticity in confined dimensions. Annu. Rev. Mater. Res. *40*, 293–317.

14. Greer, J.R., and De Hosson, J.T. (2011). Plasticity in small-sized metallic systems: intrinsic versus extrinsic size effect. Prog. Mater. Sci. *56*, 654–724.

15. Bauer, J., Meza, L.R., Schaedler, T.A., Schwaiger, R., Zheng, X., and Valdevit, L. (2017). Nanolattices: an emerging class of mechanical metamaterials. Adv. Mater. *29*, 1701850. https://doi.org/10.1002/adma.201701850.

16. Crook, C., Bauer, J., Guell Izard, A., Santos de Oliveira, C., Martins de Souza e Silva, J., Berger, J.B., and Valdevit, L. (2020). Plate-nanolattices at the theoretical limit of stiffness and strength. Nat. Commun. *11*, 1579. https://doi.org/10.1038/s41467-020-15434-2.

17. Deng, B., Xu, R., Zhao, K., Lu, Y., Ganguli, S., and Cheng, G.J. (2018). Composite bending-dominated hollow nanolattices: a stiff, cyclable mechanical metamaterial. Mater. Today *21*, 467–474. https://doi.org/10.1016/j.mattod.2018.03.027.

18. Jang, D., Meza, L.R., Greer, F., and Greer, J.R. (2013). Fabrication and deformation of three-dimensional hollow ceramic nanostructures. Nat. Mater. *12*, 893–898. https://doi.org/10.1038/nmat3738.

19. Wendy Gu, X., and Greer, J.R. (2015). Ultra-strong architected Cu meso-lattices. Extreme Mechanics Letters *2*, 7–14. https://doi.org/10.1016/j.eml.2015.01.006.

20. Shani, L., Michelson, A.N., Minevich, B., Fleger, Y., Stern, M., Shaulov, A., Yeshurun, Y., and Gang, O. (2020). DNA-assembled superconducting 3D nanoscale architectures. Nat. Commun. *11*, 5697.

21. Liu, X., Huang, J.-Q., Zhang, Q., and Mai, L. (2017). Nanostructured metal oxides and sulfides for Lithium–sulfur batteries. Adv. Mater. *29*, 1601759. https://doi.org/10.1002/adma.201601759.

22. Auyeung, E., Morris, W., Mondloch, J.E., Hupp, J.T., Farha, O.K., and Mirkin, C.A. (2015). Controlling structure and porosity in catalytic nanoparticle superlattices with DNA. J. Am. Chem. Soc. *137*, 1658–1662. https://doi.org/10.1021/ja512116p.

23. Li, Y., Tanriover, I., Zhou, W., Hadibrata, W., Dereshgi, S.A., Samanta, D., Aydin, K., and Mirkin, C.A. (2022). Monolayer plasmonic nanoframes as large-area, broadband metasurface absorbers. Small *18*, 2201171.

24. Wang, K., Ling, H., Bao, Y., Yang, M., Yang, Y., Hussain, M., Wang, H., Zhang, L., Xie, L., Yi, M., et al. (2018). A centimeter-scale inorganic nanoparticle superlattice monolayer with non-close-packing and its high performance in memory devices. Adv. Mater. *30*, 1800595. https://doi.org/10.1002/adma.201800595.

25. Lin, D., Wu, Z., Li, S., Zhao, W., Ma, C., Wang, J., Jiang, Z., Zhong, Z., Zheng, Y., and Yang, X. (2017). Large-area Au-nanoparticle-functionalized Si nanorod arrays for spatially uniform surface-enhanced Raman spectroscopy. ACS Nano *11*, 1478–1487.

26. Eivazzadeh-Keihan, R., Chenab, K.K., Taheri-Ledari, R., Mosafer, J., Hashemi, S.M., Mokhtarzadeh, A., Maleki, A., and Hamblin, M.R. (2020). Recent advances in the application of mesoporous silica-based nanomaterials for bone tissue engineering. Mater. Sci. Eng. C Mater. Biol. Appl. *107*, 110267. https://doi.org/10.1016/j.msec.2019.110267.

27. Bila, H., Kurisinkal, E.E., and Bastings, M.M.C. (2019). Engineering a stable future for DNA-origami as a biomaterial. Biomater. Sci. *7*, 532–541.

28. Xia, X., Spadaccini, C.M., and Greer, J.R. (2022). Responsive materials architected in space and time. Nat. Rev. Mater. *7*, 683–701. https://doi.org/10.1038/s41578-022-00450-z.

29. Bai, Y., Wang, H., Xue, Y., Pan, Y., Kim, J.-T., Ni, X., Liu, T.-L., Yang, Y., Han, M., Huang, Y., et al. (2022). A dynamically reprogrammable surface with self-evolving shape morphing. Nature *609*, 701–708. https://doi.org/10.1038/s41586-022-05061-w.

30. Douglas, S.M., Dietz, H., Liedl, T., Högberg, B., Graf, F., and Shih, W.M. (2009). Self-assembly of DNA into nanoscale three-dimensional shapes. Nature *459*, 414–418.

31. Rothemund, P.W.K. (2006). Folding DNA to create nanoscale shapes and patterns. Nature *440*, 297–302.

32. Douglas, S.M., Dietz, H., Liedl, T., Högberg, B., Graf, F., and Shih, W.M. (2009). Self-assembly of DNA into nanoscale three-dimensional shapes. Nature *459*, 414–418. https://doi.org/10.1038/nature08016.

33. Tian, Y., Lhermitte, J.R., Bai, L., Vo, T., Xin, H.L., Li, H., Li, R., Fukuto, M., Yager, K.G., Kahn, J.S., et al. (2020). Ordered three-dimensional nanomaterials using DNA-prescribed and valence-controlled material voxels. Nat. Mater. *19*, 789–796. https://doi.org/10.1038/s41563-019-0550-x.

34. Majewski, P.W., Michelson, A., Cordeiro, M.A.L., Tian, C., Ma, C., Kisslinger, K., Tian, Y., Liu, W., Stach, E.A., Yager, K.G., and Gang, O. (2021). Resilient three-dimensional ordered architectures assembled from nanoparticles by DNA. Sci. Adv. *7*, eabf0617.

35. Michelson, A., Zhang, H., Xiang, S., and Gang, O. (2021). Engineered silicon carbide three-dimensional frameworks through DNA-prescribed assembly. Nano Lett. *21*, 1863–1870.

36. Liu, X., Zhang, F., Jing, X., Pan, M., Liu, P., Li, W., Zhu, B., Li, J., Chen, H., Wang, L., et al. (2018). Complex silica composite nanomaterials templated with DNA origami. Nature *559*, 593–598.

37. Kosuri, S., and Church, G.M. (2014). Large-scale de novo DNA synthesis: technologies and applications. Nat. Methods *11*, 499–507.

38. Fu, Y., Zeng, D., Chao, J., Jin, Y., Zhang, Z., Liu, H., Li, D., Ma, H., Huang, Q., Gothelf, K.V., and Fan, C. (2013). Single-step rapid assembly of DNA origami nanostructures for addressable nanoscale bioreactors. J. Am. Chem. Soc. *135*, 696–702. https://doi.org/10.1021/ja3076692.

39. Tian, Y., Zhang, Y., Wang, T., Xin, H.L., Li, H., and Gang, O. (2016). Lattice engineering through nanoparticle–DNA frameworks. Nat. Mater. *15*, 654–661.

40. Oh, T., Ku, J.C., Lee, J.H., Hersam, M.C., and Mirkin, C.A. (2018). Density-gradient control over nanoparticle supercrystal formation. Nano Lett. *18*, 6022–6029. https://doi.org/10.1021/acs.nanolett.8b02910.

41. Mao, X., and Lubensky, T.C. (2018). Maxwell lattices and topological mechanics. Annu. Rev. Condens. Matter Phys. *9*, 413–433. https://doi.org/10.1146/annurev-conmatphys-033117-054235.

42. Deshpande, V.S., Ashby, M.F., and Fleck, N.A. (2001). Foam topology: bending versus stretching dominated architectures. Acta Mater. *49*, 1035–1040. https://doi.org/10.1016/S1359-6454(00)00379-7.

43. Luo, J., Wang, J., Bitzek, E., Huang, J.Y., Zheng, H., Tong, L., Yang, Q., Li, J., and Mao, S.X. (2016). Size-dependent brittle-to-ductile transition in silica glass nanofibers. Nano Lett. *16*, 105–113. https://doi.org/10.1021/acs.nanolett.5b03070.

44. Mameka, N., Wang, K., Markmann, J., Lilleodden, E.T., and Weissmüller, J. (2016). Nanoporous gold—testing macro-scale samples to probe small-scale mechanical behavior. Materials Research Letters *4*, 27–36.

45. Virwani, K.R., Malshe, A.P., Schmidt, W.F., and Sood, D.K. (2003). Young s modulus measurements of silicon nanostructures using a scanning probe system: a non-destructive evaluation approach. Smart Mater. Struct. *12*, 1028–1032. https://doi.org/10.1088/0964-1726/12/6/023.

46. Gao, H., Ji, B., Jäger, I.L., Arzt, E., and Fratzl, P. (2003). Materials become insensitive to flaws at nanoscale: lessons from nature. Proc. Natl. Acad. Sci. USA *100*, 5597–5600.

47. WIEDERHORN, S.M. (1969). Fracture surface energy of glass. J. Am. Ceram. Soc. *52*, 99–105. https://doi.org/10.1111/j.1151-2916.1969.tb13350.x.

48. Meza, L.R., Phlipot, G.P., Portela, C.M., Maggi, A., Montemayor, L.C., Comella, A., Kochmann, D.M., and Greer, J.R. (2017). Reexamining the mechanical property space of three-dimensional lattice architectures. Acta Mater. *140*, 424–432. https://doi.org/10.1016/j.actamat.2017.08.052.

49. Schaedler, T.A., Jacobsen, A.J., Torrents, A., Sorensen, A.E., Lian, J., Greer, J.R., Valdevit, L., and Carter, W.B. (2011). Ultralight metallic microlattices. Science *334*, 962–965. https://doi.org/10.1126/science.1211649.

50. Gibson, L.J. (2003). Cellular solids. MRS Bull. *28*, 270–274.

51. Silva, E.C.C.M., Tong, L., Yip, S., and Van Vliet, K.J. (2006). Size effects on the stiffness of silica nanowires. Small *2*, 239–243. https://doi.org/10.1002/smll.200500311.

52. Brambilla, G., and Payne, D.N. (2009). The ultimate strength of glass silica nanowires.

Nano Lett. *9*, 831–835. https://doi.org/10.1021/nl803581r.

53. do Rosário, J.J., Lilleodden, E.T., Waleczek, M., Kubrin, R., Petrov, A.Y., Dyachenko, P.N., Sabisch, J.E., Nielsch, K., Huber, N., Eich, M., and Schneider, G.A. (2015). Self-assembled ultra high strength, ultra stiff mechanical metamaterials based on inverse opals. Adv. Eng. Mater. *17*, 1420–1424. https://doi.org/10.1002/adem.201500118.

54. Portela, C.M., Vidyasagar, A., Krödel, S., Weissenbach, T., Yee, D.W., Greer, J.R., and Kochmann, D.M. (2020). Extreme mechanical resilience of self-assembled nanolabyrinthine materials. Proc. Natl. Acad. Sci. USA *117*, 5686–5693. https://doi.org/10.1073/pnas.1916817117.

55. Bauer, J., Schroer, A., Schwaiger, R., and Kraft, O. (2016). Approaching theoretical strength in glassy carbon nanolattices. Nat. Mater. *15*, 438–443. https://doi.org/10.1038/nmat4561.

56. Liu, X., Jing, X., Liu, P., Pan, M., Liu, Z., Dai, X., Lin, J., Li, Q., Wang, F., Yang, S., et al. (2020). DNA framework-encoded mineralization of calcium phosphate. Chem *6*, 472–485. https://doi.org/10.1016/j.chempr.2019.12.003.

Cell Reports Physical Science, Volume *4*

Supplemental information

High-strength, lightweight nano-architected silica

Aaron Michelson, Tyler J. Flanagan, Seok-Woo Lee, and Oleg Gang

Contents

A

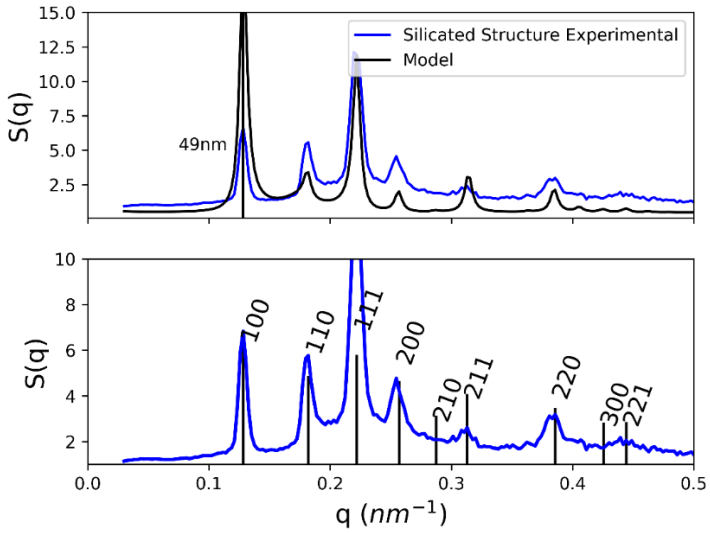

B

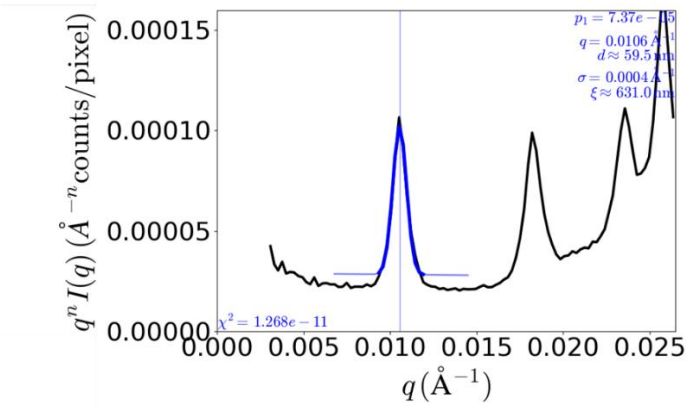

Figure S1. Small Angle X-ray Scattering of DNA origami Lattice

Small angle X-ray scattering measurements carried out at the Complex Matter Scattering (CMS) beamline at the National Synchrotron Light Source II (NSLSII). The experimental data is plotted against a model of a simple cubic lattice with a lattice parameter matching the first peak of the structure at q = 0.128 nm^{-1} or 49nm. The correlated growth can be obtained from a fitting of the first peak shown in B.

A) Top: Small angle X-ray scattering of silica coated DNA nanolattice framework (blue) and modelled scattering (black) from ScatterSim CFN-softbio/ScatterSim: Meso scale SAXS Powder Simulations (github.com) Bottom: Zoomed in region with scattering peak *hkl* demarked for the Simple cubic superlattice. B) Gaussian peak fitting for the DNA framework nanolattice (before templating with silica) on (100) *hkl* peak with correlation length of ~600nm from the Scherrer equation.

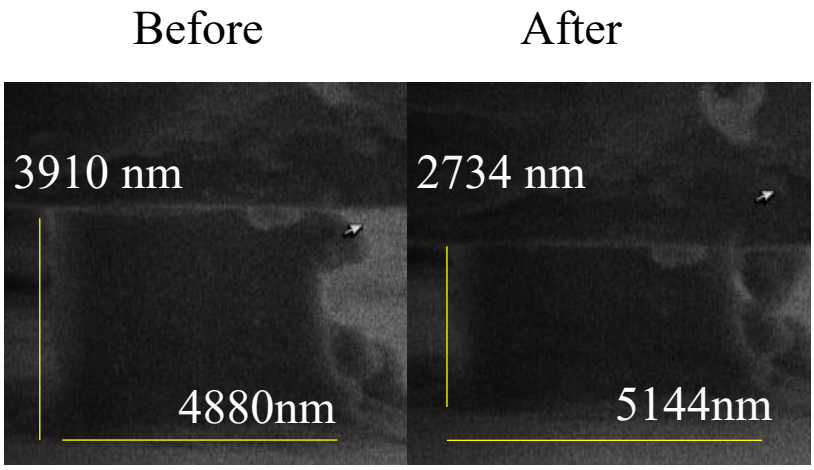

$$v = -d\frac{d\epsilon_z}{d\epsilon_x} = 0.22$$

Figure S2. Poisson Ratio Calculation.

Poisson Ratio as calculated from SEM microscopy before and after indentation

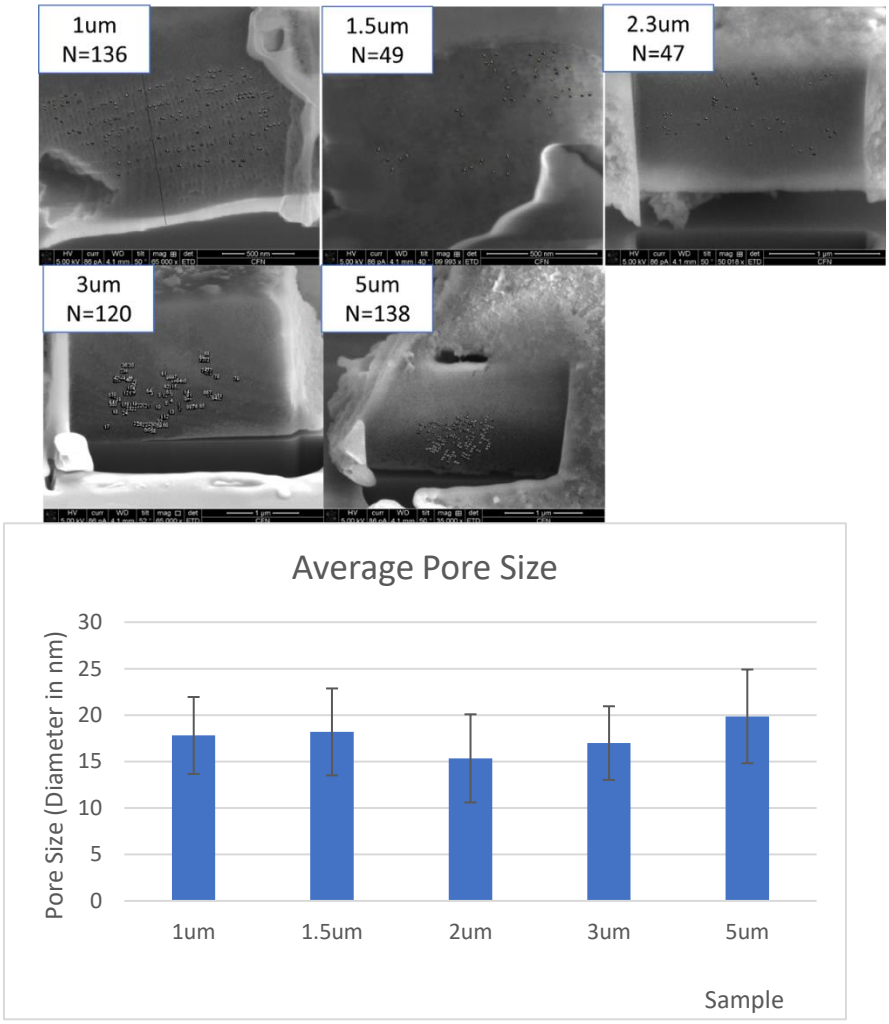

Figure S3. Pore Size Evaluation of Superlattices via FIB/SEM Sections.

Top: FIB/SEM image of superlattices with markers representing locations that were measured using ImageJ for comparison. Bottom: Pore size diameter vs sample size demonstrating between 15-20nm diameter which translates to ~20nm strut diameter.

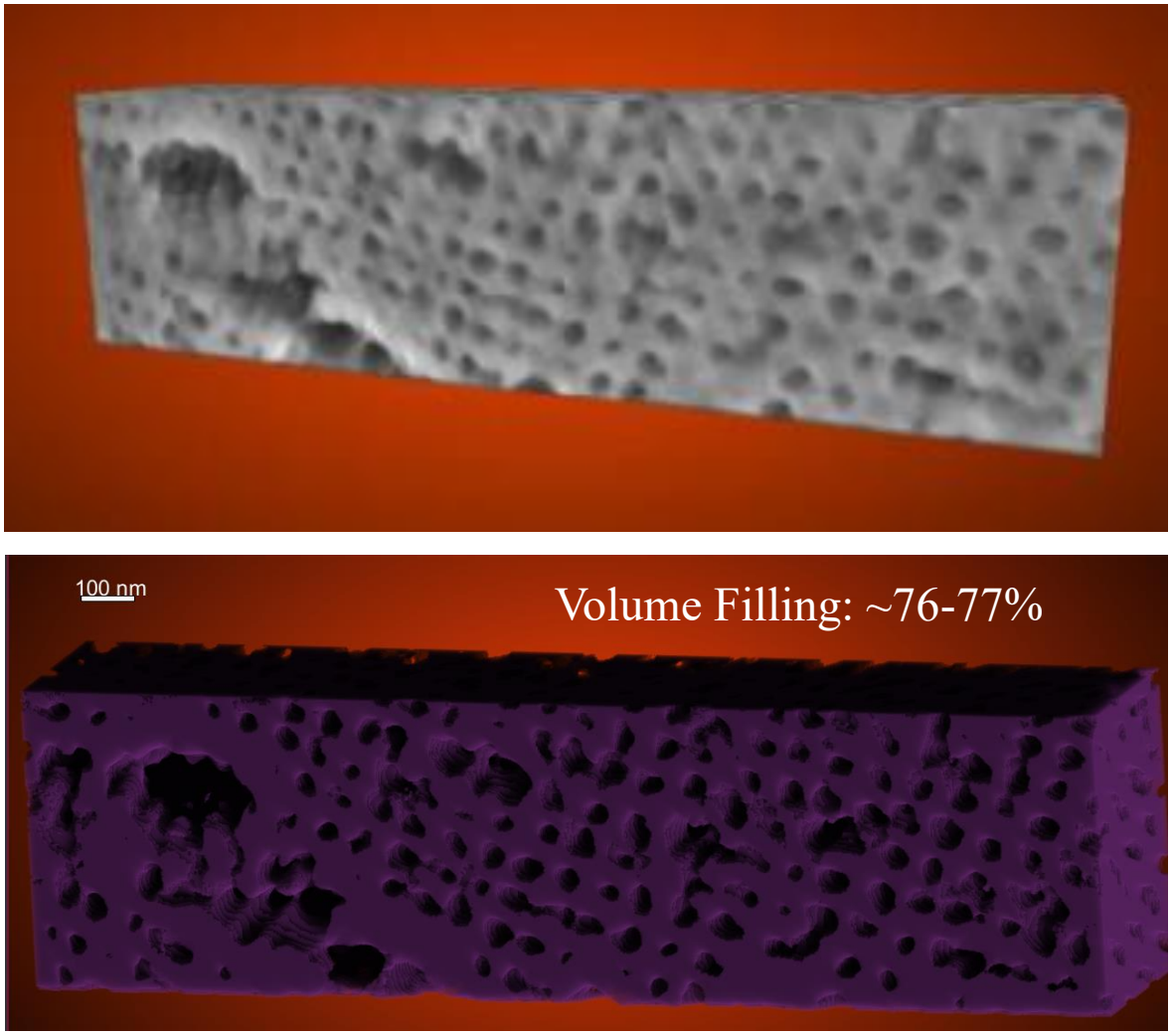

Figure S4. 3D Reconstruction from FIB/SEM Serial Sectioning.

Top: Gray scale image of the probed volume, reconstructed from 5-7nm slices. Bottom: A volume of the superlattice used for the calculation of effective solid fraction. The lattice was then segmented into pore space and sample using Dragonfly Software Dragonfly | 3D Visualization and Analysis Solutions for Scientific and Industrial Data | ORS (theobjects.com) The internal volume was calculated compared to the total pixel volume. Total Volume: 19e6 pixels: 0.55 μm^3 . Upper Otsu Thresholding: 66% filled labeled volume: 12e6 pixel volume: Discretionary Thresholding: 77% 15e6 pixels: 0.42 μm^3

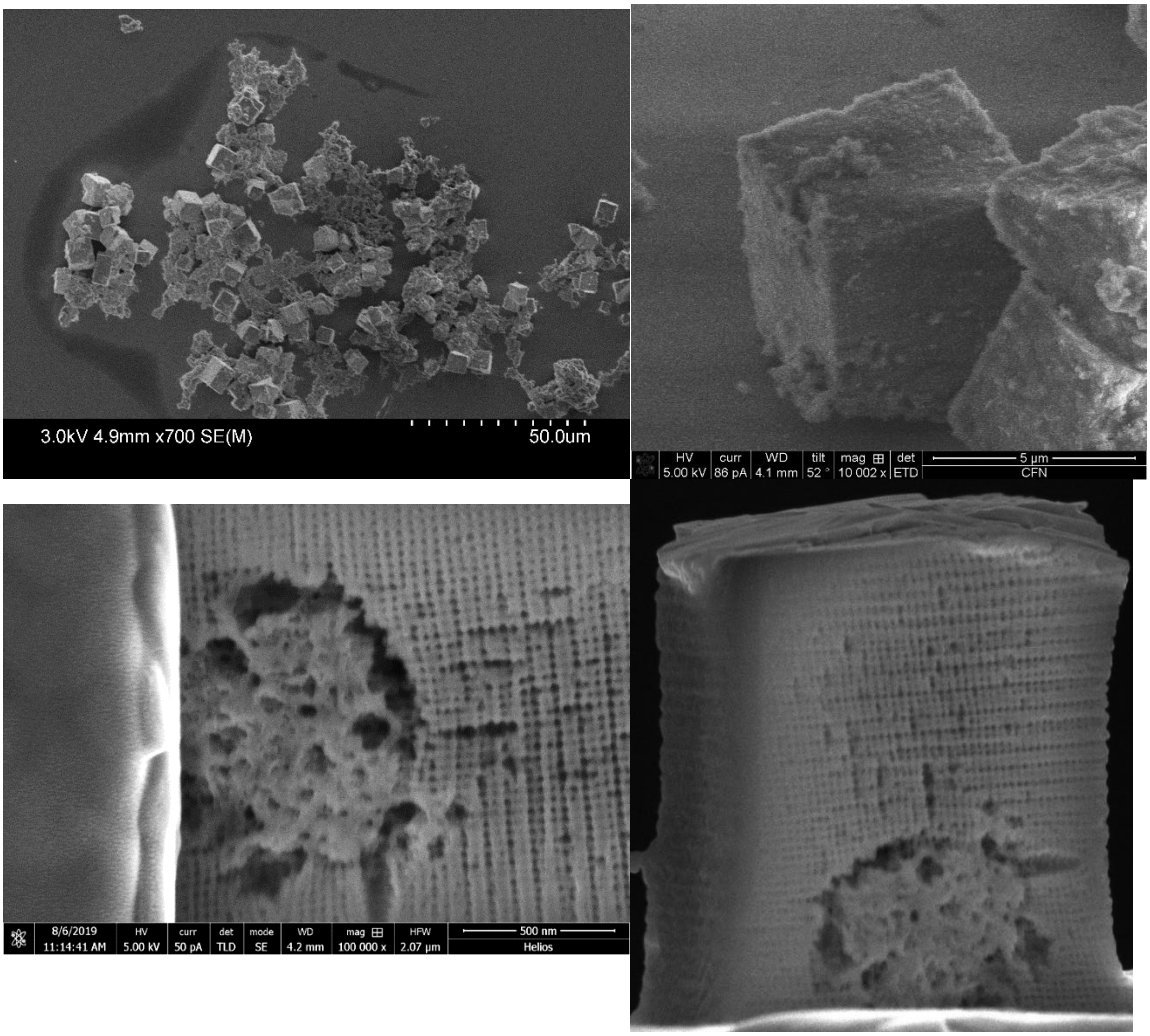

Figure S5. Additional SEM of Nanolattices.

As an example of the type of defects that can occur in the superlattice which are not apparent from the surface are amorphous regions internal to the superlattice structure, this most likely originates as a grain with a different orientation or defective agglomeration of DNA material. These types of defects would not be expected within the correlation length of 1um. This is a likely cause for brittle fracture in the superlattice.

Top Left: Low Magnification (700x) of a cluster of superlattice with cubic geometry on a Silicon wafer. Top Right: 10kx Image of a superlattice standing upright on the silicon wafer. Bottom-left/right: High Resolution SEM of defects in the superlattice as imaged using Fib/SEM for serial sectioning.

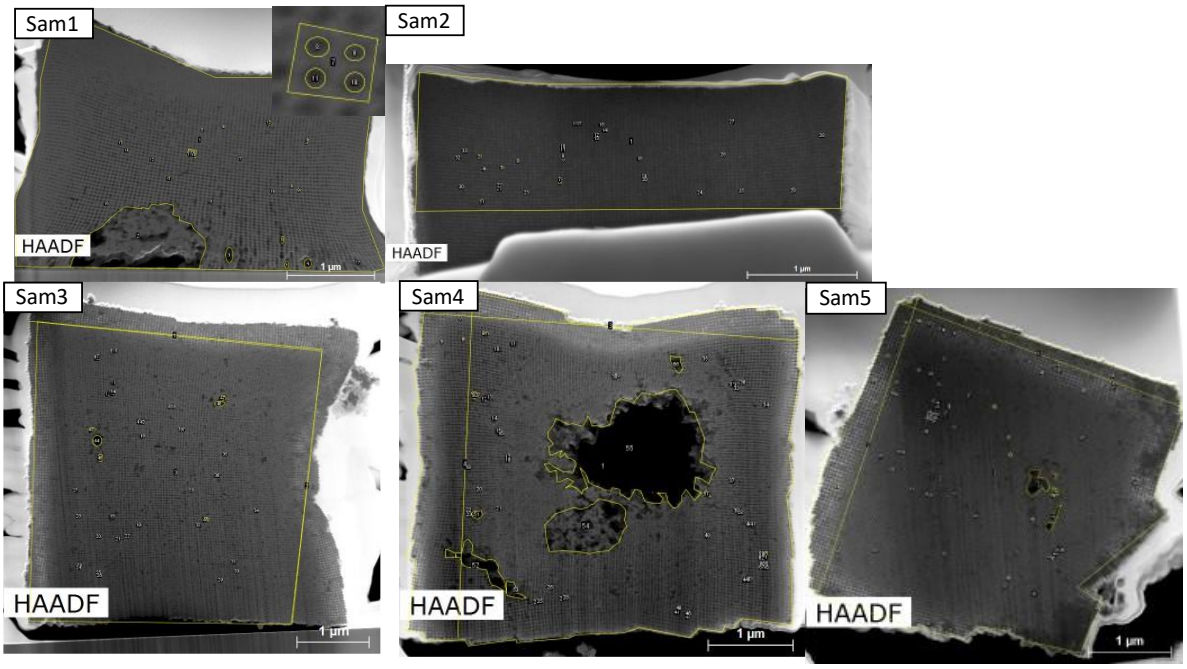

Figure S6. Fib/TEM Cross sections of Silicated Samples.

The FIB/SEM was used to prepare cross sections of 5 samples which were then analyzed (ImageJ) for the number of vacancies and pore volume compared to the total number of octahedra estimated from using the octahedral unit length and subdividing the large area. Samples 1 and 4 demonstrate significant pores/defect volumes not apparent from the exterior SEM. See Table S2 for quantification from the above images.

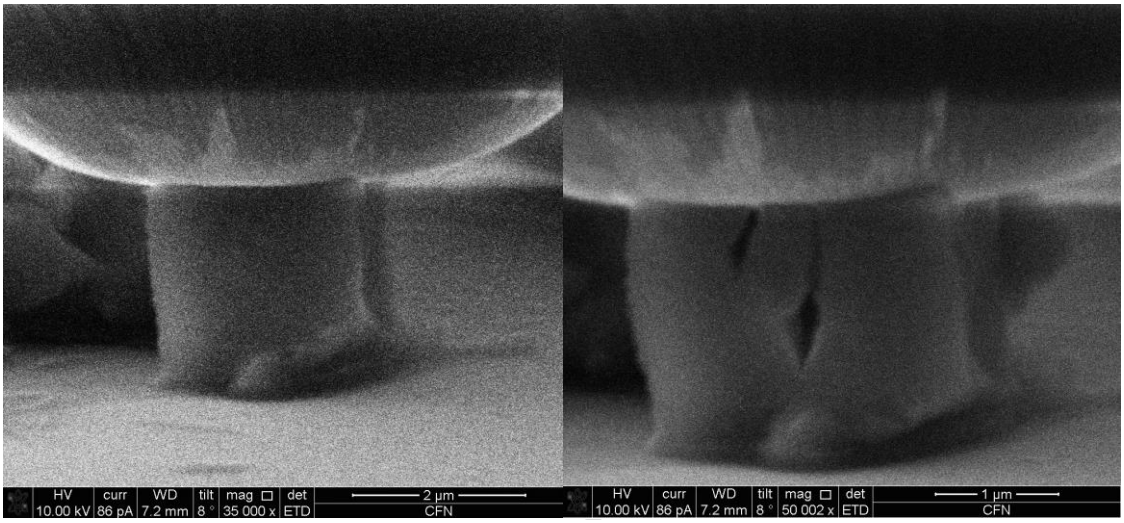

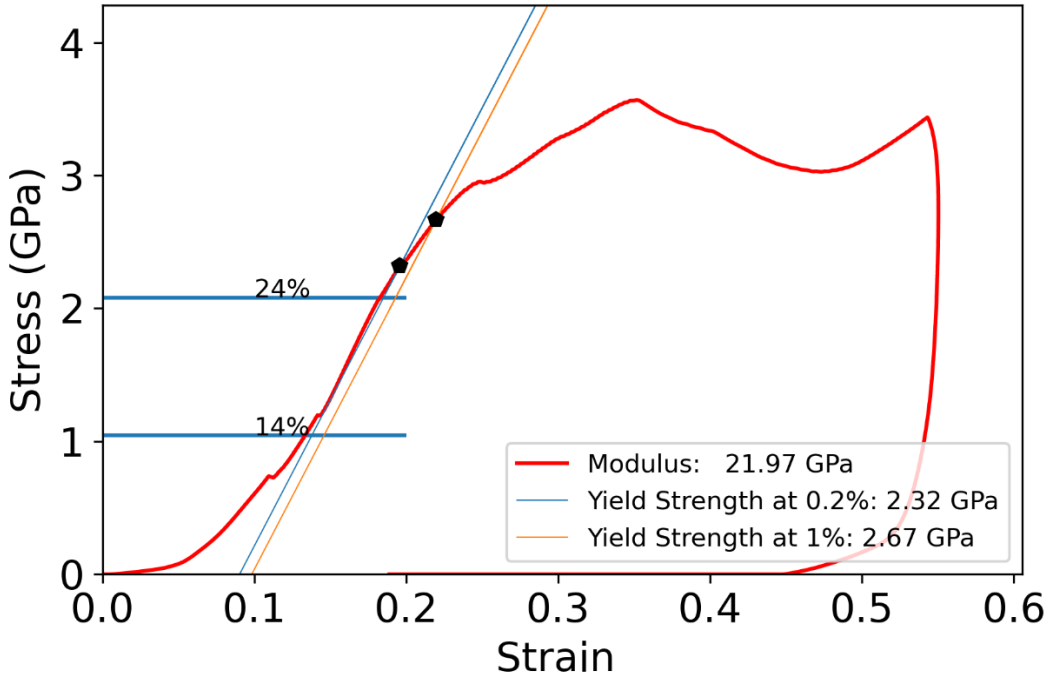

Figure S7. Barreling and Lateral Tensile Cracking.

SEM of superlattice (Left) prior and (Right) during indentation. It can be seen in the right image that the lattice barrels out and a crack develops in a central portion cleaving through lattice planes. The accompanying stress-strain curve is plotted below. The Blue lines represent the fitted region of the curve for the 0.2% and 1% yield strength offset.

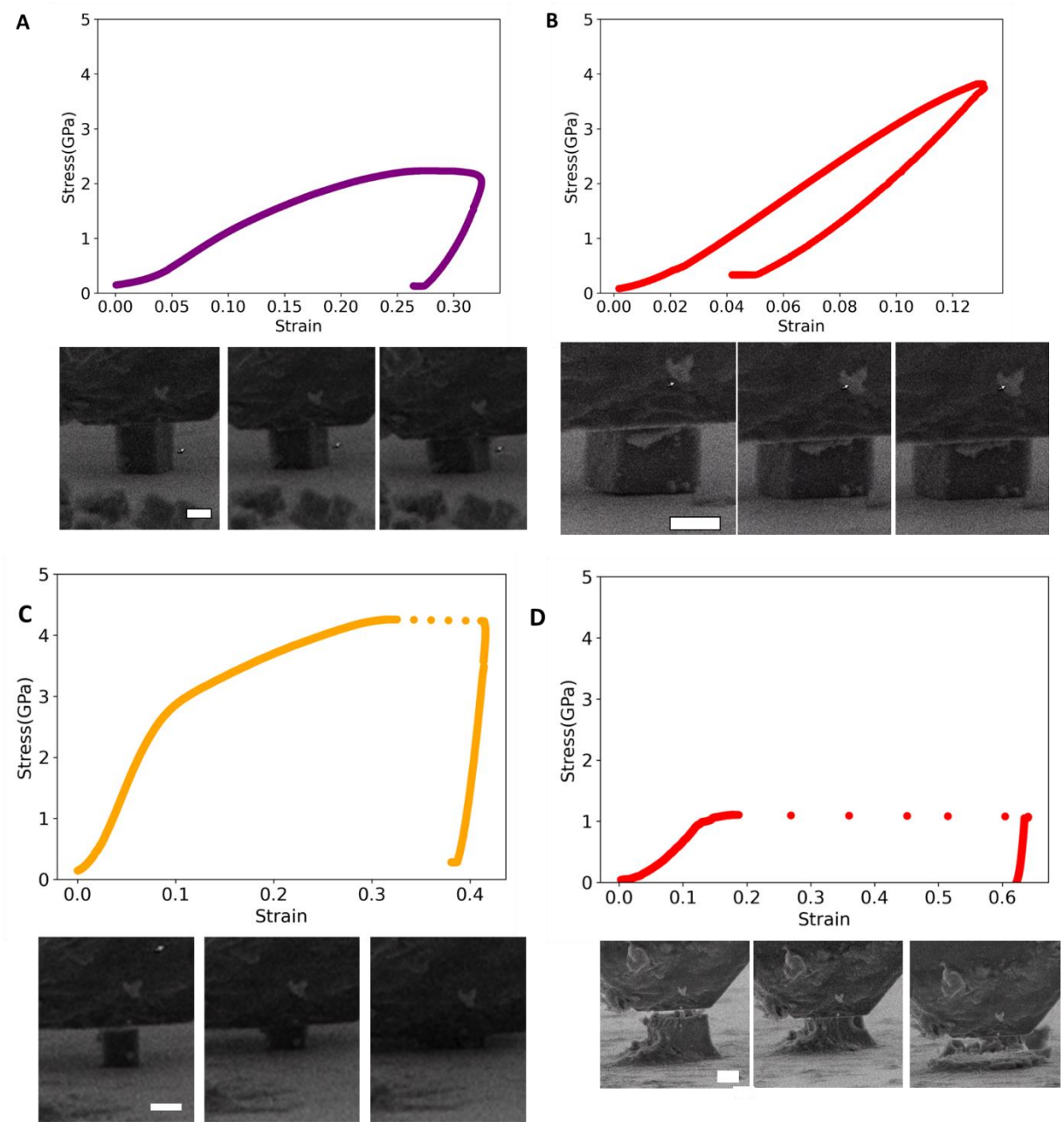

Figure S8. Additional In-situ Stress/Strain Curves for Ductile and Brittle Nanolattices.

Ductile (A+B) and Brittle (C+D) stress strain curves with still shots from in-situ video taken during the collection.

Table S1. Mechanical Properties of Silica Nanolattice. A summary of measured silica nanolattices of different edge lengths

Edge Length	Youngs Modulus (GPa)	E/E_bulk	Yield Strength at 0.2% strain (GPa)	Yield Strength at 1% strain offset (Gpa)
1.25	32.19	0.45	3.95	4.53
1.5	34.43	0.48	2.8	3.42
1.8	22.52	0.32	2.79	3.13
2	37.22	0.52	2.34	2.76
2	18.99	0.27	3.56	4.1
2	12.23	0.17	2.71	2.84
2	6.41	0.09	2.53	2.53
2.2	27.88	0.39	1.85	2.54
2.3	14.13	0.20	4.43	4.83
2.3	21.97	0.31	2.32	2.67
2.5	27.02	0.38	2.27	2.64
2.5	19.03	0.27	2.59	2.86
2.7	12.98	0.18	1.86	2.2
2.9	27.48	0.39	2.38	2.9
3	35.76	0.50	3.19	3.82
3.2	10.25	0.14	0.99	1.15
3.2	17.61	0.25	1.91	1.76
3.5	13.09	0.18	1.18	1.49
3.5	17.95	0.25	1.45	1.66
3.5	27.6	0.39	2.29	2.71
3.62	3.72	0.05	0.67	0.95
3.8	20.24	0.29	1.13	1.27
4	17.63	0.25	1.63	2.04
4.5	13.84	0.19	1.21	1.34
4.5	13.17	0.19	0.47	0.57
4.8	15.21	0.21	1.75	1.87
5	3.8	0.05	0.506	
6	9.95	0.14	1	1.07
7.5	16.2	0.23	1.26	0.91

Unit(s)	Parameter	Sam1	Sam2	Sam3	Sam4	Sam5
	Length (nm)	3844	3906	4094	4400	3520
	Width (nm)	2838	1164	3823	4062	3664
octahedra	Octa tot units length	174.7273	177.5455	186.0909	169.2308	95.13514
octahedra	octa tot units width	129	52.90909	173.7727	156.2308	99.02703
	Octahedral Width (nm)	22			26	37
units	Vacancies (count)	17	32	40	45	76
	Vacancy Rate	0.000754	0.003407	0.001237	0.001702	0.008067
octahedra	Total Octa (calc)	22539.82	9393.769	32337.52	26439.05	9420.95
nm^2	Total Area	9497219	4547510	15452647	20929202	12573578
	Ideal Filling Factor	0.757	0.75	0.769	0.73-0.8	0.695
	Defective Filling Factor (pores, vacancies)	0.658	0.744371	0.764	0.617-0.68	0.686
Void space		9.0%	0.0%	0.3%	11.0%	0.6%

Table 2. Summary of Fib/TEM Cross Section Analysis. See Figure S6 for images. Octahedral unit width was constant for sample 2 and sample 3, the deviation in sample 5 may have to do with a slightly different angle of the cut sample.

Note S1. DNA Sequences Reference

Tian, Ye, et al. "Lattice engineering through nanoparticle–DNA frameworks." *Nature materials* 15.6 (2016): 654-661. They can also be provided by the authors upon request.